



Human urine-derived stem cell exosomes delivered via injectable GelMA templated hydrogel accelerate bone regeneration



Wei Lu^{a,c,1}, Min Zeng^{a,c,1}, Wenbin Liu^{a,c}, Tianliang Ma^{a,c}, Xiaolei Fan^d, Hui Li^b,
Yinan Wang^{a,c}, Haoyi Wang^{a,c}, Yihe Hu^{a,b,*}, Jie Xie^{a,b,**}

^a Department of Orthopedic Surgery, National Clinical Research Center of Geriatric Disorders, Xiangya Hospital, Central South University, Changsha, China

^b Department of Orthopedics, The First Affiliated Hospital, Medical College of Zhejiang University, Hangzhou, China

^c Hunan Engineering Research Center of Biomedical Metal and Ceramic Implants, Changsha, China

^d Department of Orthopedics, Honghui Hospital, Xi'an Jiaotong University, Xi'an, China

ARTICLE INFO

Keywords:

Bone regeneration
Exosomes
H-type vessels
GelMA
HAMA

ABSTRACT

The key to critical bone regeneration in tissue engineering relies on an ideal bio-scaffold coated with a controlled release of growth factors. Gelatin methacrylate (GelMA) and Hyaluronic acid methacrylate (HAMA) have been a novel topic of interest in bone regeneration while introducing appropriate nano-hydroxyapatite (nHAP) to improve its mechanical properties. And the exosomes derived from human urine-derived stem cells (human ^{USC}EXOs) have also been reported to promote osteogenesis in tissue engineering. The present study aimed to design a new GelMA-HAMA/nHAP composite hydrogel as a drug delivery system. The ^{USC}EXOs were encapsulated and slow-released in the hydrogel for better osteogenesis. The characterization of the GelMA-based hydrogel showed excellent controlled release performance and appropriate mechanical properties. The in vitro studies showed that the ^{USC}EXOs/GelMA-HAMA/nHAP composite hydrogel could promote the osteogenesis of bone marrow mesenchymal stem cells (BMSCs) and the angiogenesis of endothelial progenitor cells (EPCs), respectively. Meanwhile, the in vivo results confirmed that this composite hydrogel could significantly promote the defect repair of cranial bone in the rat model. In addition, we also found that ^{USC}EXOs/GelMA-HAMA/nHAP composite hydrogel can promote the formation of H-type vessels in the bone regeneration area, enhancing the therapeutic effect. In conclusion, our findings suggested that this controllable and biocompatible ^{USC}EXOs/GelMA-HAMA/nHAP composite hydrogel may effectively promote bone regeneration by coupling osteogenesis and angiogenesis.

1. Introduction

Critical bone regeneration remains a major challenge in the orthopedic field, usually treated by bone grafting, Ilizarov bone transportation, the Masquelet technique, and tissue engineering [1]. While many treatments are available, there is no preferred treatment prescription. One strategy of growing interest in recent years is tissue-engineered bone grafts, owing to their advantages of unlimited supply and lack of disease transmission. In bone tissue engineering, the key to bone regeneration relies on an ideal bio-scaffold, which provides a biodegradable scaffold

for osteoconduction, a controlled release of growth factors for osteoinduction, and progenitor cells for osteogenesis [2].

Recently, the active participation of progenitor cells and growth factors greatly contributes to the process of bone regeneration [3]. Exosomes have been found to contain various lipids, proteins, and nucleic acids, which play important roles in cell-to-cell communication and cellular immune reactions [4]. Notably, cells have been successfully isolated and cultivated from urine [5]. The morphology of these cells is epithelioid and long spindle-shaped. Similarly, such cells have been identified as being able to express stem cell markers and have

* Corresponding author. Department of Orthopedic Surgery, National Clinical Research Center of Geriatric Disorders, Xiangya Hospital, Central South University, Changsha, China.

** Corresponding author. Department of Orthopedic Surgery, National Clinical Research Center of Geriatric Disorders, Xiangya Hospital, Central South University, Changsha, China.

E-mail addresses: skak685985@163.com (W. Lu), xy_zengmin@163.com (M. Zeng), xy_huyh@163.com (Y. Hu), dr_xiejie@zju.edu.cn (J. Xie).

¹ These authors contributed equally to this work and share first authorship.

multifunctional differentiation potentials [6–8]. Zhang et al. have also identified a subpopulation of urothelial cells that express stem cell markers and possess potentiation for multiple differentiation [9]. We have previously demonstrated that human urine-derived stem cell exosomes (human ^{USC}EXOs) have multifunctional differentiation potential under in vitro culture conditions. These exosomes have also been shown to suppress osteolysis and promote osteogenesis [10,11].

One of the challenges in the therapeutic application of exosomes is their delivery method, with the most common mode including systemic, local injection, intrathecal, and intranasal delivery mechanisms [12–14]. These methods have serious weaknesses, which require the consumption of large amounts of exosomes, besides the exposure of the delivery pathway to “bystander” tissues, which leads to the inefficiency and the enhancement of ectopic effects [15]. The repair of bone tissue damage is a long-term, complex, multi-stage process. Inappropriate exosome delivery vehicle, which may limit the effect. Therefore, selecting a prospective exosome delivery system to load exosomes may be an appropriate therapeutic strategy for bone repair. To overcome this challenge, exosomes are allowed to be loaded in a hydrogel, which increases the stability and retains the ability of exosomes in vivo and maintains a biological role around the injury. For some scenarios, photocrosslinkable hydrogel becomes a popular new treatment tool for orthopedists. The ability of chemical photo-crosslinking to rapidly form hydrogel networks under mild conditions and ambient temperatures is one of the major advantages. The most employed strategy for cross-linking is the adoption of polymers (naturally derived or synthetic) modified with reactive groups that can carry out polymerization chain reactions (methacrylate and/or methacrylamide) [16,17].

Gelatin methacrylate (GelMA) can undergo rapid photo-crosslinking due to the methacrylation of amino and carboxyl groups on the gelatin side chain. In addition, it conserves the Arg-Gly-Asp (RGD) sequence and enzymatic degradability of gelatin's cell interaction-promoting groups, which enables improved cell adhesion, promotes cell growth and proliferation, and regulates cell viability [18,19]. Consequently, GelMA is commonly used in 3D cell culture to study cell proliferation, migration, differentiation, and tissue engineering. Pure GelMA hydrogels, however, have poor mechanical properties and a relatively fast degradation rate [20,21]. Hyaluronic acid methacrylate (HAMA) has also been explored as a photocrosslinkable hydrogel, and Hyaluronic acid is an essential extracellular matrix in adult heart valves and skin. Its degradative properties are slowness, which may increase the structural integrity of the hydrogel for prolonged experiments. Fan et al. added HAMA to GelMA hydrogel in order to obtain a composite hydrogel with reinforced mechanical properties for 3D printing [22]. Nevertheless, HAMA hydrogels exhibit limited cell adhesion, which may lead to limited cell spreading capacity [23,24]. Nano hydroxyapatite (nHAP), the main inorganic component of the natural bone matrix, has been demonstrated to have biological activity in directing and inducing bone formation. In addition, nHAP deposition into the GelMA network also enhances the stiffness of GelMA hydrogel as a whole [25,26]. Gao et al. designed a series of GelMA and GelMA-hydroxyapatite bilayer hydrogels by 3D printing which possessed excellent cartilage regeneration ability with cartilage lacunae and subchondral bone formation in a rabbit bone soft regeneration model [27].

Previous studies have revealed that HAMA combined with nHAP and GelMA has improved mechanical properties and biocompatibility [1,28]. Liu et al. prepared hydrogels based on GelMA and HAMA as drug delivery systems for osteochondral defect repair in the rabbit knee joint [29]. Li et al. suggest that the introduction of GelMA to construct hybrid hydrogels (HAMA-GelMA), compared with GelMA or HAMA single network hydrogels, demonstrates that the hybrid hydrogels possess appropriate physical properties and show desirable effects on cell viability, adhesion, and cell spreading [20]. Zuo et al. designed a modular hydrogel based on GelMA and nHAP for application in bionic bone-form units. These composite hydrogels possess a low swelling rate, high mechanical strength, and better biocompatibility than pure GelMA hydrogels [26].

Therefore, the degree of densification in the fibril network can be reinforced by incorporating HAMA hydrogel and nHAP into GelMA hydrogel rather than using GelMA hydrogel alone.

Given the above background, we aimed to design a GelMA-HAMA/nHAP composite hydrogel to develop a drug delivery system. The human ^{EXO}USCs were encapsulated in the hydrogel for osteogenesis. The scaffold was systematically characterized to evaluate its physical properties, release rate, and osteogenesis and angiogenesis capability in vitro. Then, the in vivo bone repair efficacy was evaluated using a cranial bone defect model in rats. Our research provided deep insight into the design of controllable and biocompatible GelMA-based hydrogels and offered an effective therapeutic approach for critical bone regeneration (Scheme 1).

2. Materials and methods

2.1. Materials

GelMA, HAMA and lithium phenyl-2,4,6-trimethylbenzoylphosphonate (LAP) were purchased from SunP Boyuan Biotech Co., Ltd (Beijing, China). NHAP was purchased from Sigma-Aldrich (MO, USA). Osteogenic induction medium and Alizarin Red Staining (ARS) kit were purchased from Cyagen Biosciences (Guangzhou, China). Fetal bovine serum was purchased from Moregate Biotech Co., Ltd (Bulimba, Australia). Dulbecco's modified Eagle's medium (DMEM) and Trypsin were obtained from Gibco (Grand Island, USA). DMEM/F-12 supplemented with the REGM SingleQuot kit was bought from Lonza (USA). All the Cytokines were bought from Peprotech (Rocky Hill, USA). All the antibodies were bought from Proteintech Group Inc (Wuhan, China). Crystalline violet staining kit, DAPI and FITC were purchased from Solarbio Life Sciences (Beijing, China). Total protein assay kit, Cell Counting Kit-8(CCK8) kit, Alkaline Phosphatase (ALP) staining kit, DiI Fluorescent Staining Kit, DiR Fluorescent Staining Kit and Calcein-AM/PI staining kit was purchased from Beyotime Biotechnology (Shanghai, China). Crystalline violet reagent purchased from Solarbio Life sciences (Beijing, China). Growth factor-reduced Matrigel was purchased from BD Bioscience (Shanghai, China). Steady-Pure Universal RNA Extraction Kit, Evo M-MLV RT Premix Kit and SYBR® Green Premix Pro Taq HS qPCR Kit were purchased from Accurate Biology (Changsha, China).

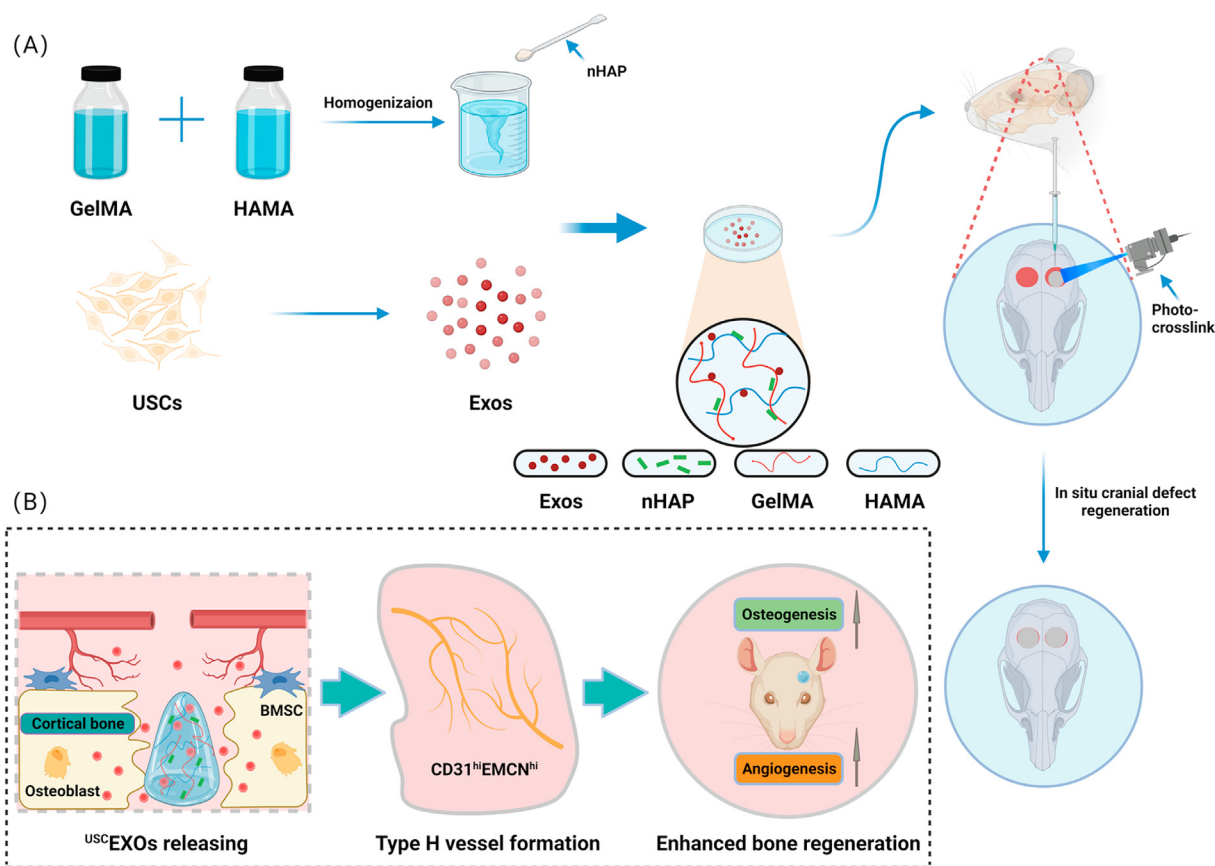
2.2. Preparation of composite hydrogels

Initially, different proportions of HAMA, GelMA, and nHAP powder particles were added to double-distilled water and magnetically stirred for 1 h at 60 °C under water bath heating conditions avoiding light. Table 1 shows the composition and abbreviations of the hydrogels in this study. Then, the sufficiently stirred hydrogel solution was subject to ultrasonic stirring whereby the nHAP particles were homogeneously separated within the hydrogel solution, followed by the addition of 0.1% v/v LAP for 2 min under 405 nm wavelength illumination for photocrosslinking.

2.3. Characterization of composite hydrogel

The spectra of pure GelMA, HAMA and composite GelMA—HAMA (G₅H₂) were obtained by a ¹H Nuclear Magnetic Resonance system (¹H NMR, BrukerAVIII500 M, Switzerland) at room temperature. Firstly, the methacrylic acid biopolymer samples were photocrosslinked under illumination (405 nm). Then, these samples were Lyophilized to remove excess liquid prior to dissolving in D₂O (30 mg/ml), following the above solution was characterized by determining its degree of methacrylation.

The chemical properties of the hydrogels photocrosslinked were characterized by Fourier transform infrared spectroscopy (FTIR). Data acquisition was performed using an FTIR spectrometer (Varian 670, Agilent, Santa Clara, CA, USA) connected to a plotting microscope (Varian 620-IR, Agilent, Santa Clara, CA, USA). Samples were obtained at samples were analyzed in the interval from 400 to 4000 cm⁻¹ with a



Scheme 1. Novel photocrosslinked hydrogels combined with human urine-derived stem cell exosomes have substantial merits in osteogenic repair. (A) Procedures for preparation of composite hydrogels. (B) Novel photocrosslinked hydrogels with instantaneous in situ seamless adhesion adapted to various bone defect morphologies and retaining human urine-derived stem cell exosome function to initiate osteogenesis and angiogenesis for cranial bone regeneration in rats.

Table 1

The composition of different composite hydrogel.

Samples	Composition (% w/v)		
	GelMA	HAMA	nHAP
G ₅ H ₁	5%	1%	0.5%
G ₅ H _{1.5}	5%	1.5%	0.5%
G ₅ H ₂	5%	2%	0.5%

spectral resolution of 4 cm⁻¹ with 64 scans per minute and a total of 100 scans per spectrum.

The morphology of the hydrogels had an impact on their mechanical strength and was characterized. G₅H₁, G₅H_{1.5}, and G₅H₂ hydrogels were freeze-dried in a vacuum at 80 °C, ruptured from the center and sprayed with Pt for 60 s. The porous structure of the truncated surface of the hydrogel scaffolds was identified with a tungsten scanning electron microscope (SEM, MERLIN, Carl Zeiss, Germany).

The rheometer (HAAKE, MARS60, Germany) is equipped with a 25 mm diameter plate having a gap distance of 1 mm to measure the rheological properties of laminating inks. The kinetic viscosity (0.1–1000 s⁻¹) and the temperature sweep (1 s⁻¹, 10–40 °C) with constant strain and frequency were performed at room temperature to investigate the viscosity properties of the hydrogels for various hydrogels, respectively. Real-time changes in the energy storage modulus (*G'*) and loss modulus (*G''*) of hydrogels at room temperature during free-radical polymerization were measured by oscillation frequency. The modulus of the hydrogel was measured by an oscillatory sweep at a constant frequency (10 rad s⁻¹; 0.1–100% strain) and frequency sweep at a constant strain

(1% strain; 0.01–100 rad s⁻¹). In these cases, the relationship between the deformation behavior of the hydrogel and the composition ratio was investigated.

The compression properties of the hydrogels were evaluated on an Instron IBTC-3000SL (Care Measurement & Control Co. Ltd, Beijing, China). Various group hydrogels were prepared as cylinders (Φ 8 mm × 8 mm) for testing, and samples (n = 3) were submerged in distilled water to reach swelling equilibrium. The hydrogels were tested at a constant compression rate of 0.1 mm/min. The compressive modulus of all hydrogels was calculated by calculating the gradient of the initial linear stress-strain curve region.

The USC EXOs labelled with DiI red fluorescent dye (200ug) were mixed with hydrogels according to Table 1 (n = 3) and then photocrosslinked using a blue light-emitting (405 nm) light source (SunP, Beijing, China). The percentage of exosomes sustained release was calculated by measuring the fluorescence intensity of the exosomes released at the defined time points. The fluorescence intensity was measured using a multifunctional enzyme marker (ENVISION2105, PerkinElmer, USA). subsequently, each well was given a new PBS solution to submerge the hydrogel, and the cumulative release curve was documented and plotted.

Each hydrogel (Φ 5 mm × 5 mm) was immersed in 1 mL double-distilled water at a constant temperature of 37 °C to verify the swelling behavior of hydrogels (n = 3). Hydrogels were removed to record wet weight (*W_t*), measured within one day of collection. Each hydrogel was weighed before immersion and recorded as *W₀*. The swelling rate was calculated using the following equation: (*W_t* - *W₀*)/*W₀* × 100%. Each group measured three parallel specimens.

2.4. Isolation and identification of exosomes

Extraction and purification of exosomes from human urine-derived stem cells were referenced from previous studies [10,11]. Briefly, upon 70–80% confluence of the human urine-derived stem cells (passage 3) in the 25 T culture flask, replace the medium depotted exosome and incubate for 48 h. The medium collected above was followed by the centrifugation step to remove cell debris: 2000g for 30 min, then filtration with a 0.22 μm spout for subsequent experiments. The supernatant was added to an Amicon Ultra-15 Centrifugal Filter Unit (100 kDa; Millipore) and centrifuged at 4000 g for 20 min. The one-fifth volume of Exoquick Exosome Precipitation Solution (System Biosciences, USA) was added to the ultrafiltrate and homogenized by blowing with a 200ul TIP for 12 h at 4 °C. After incubation for 12 h, The mixture was subjected to centrifugation for 30 min (1500 g, 4 °C), and the supernatant was removed. The precipitate was finally resuspended with 200 μl PBS solution along with the BCA method, which was stored at minus 80 °C.

The particle size of exosomes was measured by the Nanoparticle Tracking Analysis (NTA, Particle Mtrix, Meerbusch, Germany). Measurements and analyses of the NTA were conducted at 11 locations. In addition, exosomes morphology were observed by transmission electron microscopy (TEM) according to the published protocol [30]. Detection of TSG101 (ab125011; Abcam), CD63 (sc-5275; Santa) and calnexin (ab22595; Abcam) in exosomes was performed by western blotting [11].

2.5. CCK8 assay and live/dead cell staining

The hydrogels were co-cultured with 1×10^4 rat BMSCs and EPCs planted in 96-well plates, respectively. Cell proliferation was detected at time points of days 1, 2, and 3 using the CCK8 kit. The seeded cells were washed three times with deionized water and incubated in CCK-8 reagent (10% dilution in culture medium) for 1 h. The mixture was collected at 450 nm to measure absorbance with a microplate reader (BiotekEpoch, USA). Besides, Live/dead assays were then performed. The co-culture was continued for 24 h in 24-well plates, after which 100 μl of live/dead staining solution was added. Subsequently, cells were incubated in darkness at 37 °C for 30 min. Fluorescent images of live/dead cells were captured by the confocal laser scanning microscope (SP8-DMIL, Leica, Germany) and processed with Image J software.

2.6. Internalization assay in vitro

The USC^{EXO} s were incubated with DiI red fluorescent dye for 30 min at 37 °C in darkness according to the manufacturer's instructions. Then, the exosomes suspension was added to an ultrafiltration tube (100 kDa) for centrifugation for 30 min (10,500 rpm, 4 °C), and the supernatant was discarded. The labelled exosomes were added to the BMSCs and EPCs and incubated for 12 h. Following this, cells were washed with deionized water and fixed with 4% paraformaldehyde for 15 min. Next, the cytoskeleton was stained with FITC for 30 min, and the nuclei were stained with DAPI for 1 h at room temperature, shielded against the light. Finally, the signals were analyzed by the confocal laser scanning microscopy (AirScan, Zeiss, Germany).

2.7. Alkaline phosphatase and Alizarin Red staining

The G_5H_2 composite hydrogel with USC^{EXO} s (50ug) was used for experiments. For Alkaline Phosphatase staining, after 3 days of co-culture, BMSCs (1×10^5) cultured on well plates were washed 3 times with deionized water, incubated with alkaline phosphatase staining reagent for 30 min at room temperature, and finally washed again with deionized water 1 time before observation under the inverted light microscope (Ti2-A, Nikon, Japan).

After 14 days of osteogenic induction, for Alizarin Red staining, BMSCs at the bottom of the plates were fixed with 4% paraformaldehyde at room temperature for 30 min prior to washing 3 times with deionized

water. BMSCs (4×10^4) were stained with Alizarin Red S for 20 min after cell fixation. Finally washed again with deionized water 1 time before observation under the inverted light microscope (Ti2-A, Nikon, Japan).

2.8. Tube formation assay

To verify the effect of USC^{EXO} s/ G_5H_2 composite hydrogels on the activity of EPCs, the formation of nascent tubule-like structures was performed. EPCs (3×10^4) were inoculated onto Matrigel-coated 48-well plates (110ul/well) and incubated in mixed media containing 50ug USC^{EXO} s. After 5 h, bright images of each well were observed and photographed under the inverted light microscope (Ti2-A, Nikon, Japan). ImageJ software determined the relevant parameters (total length, Number of Branches, Number of Junctions) involved in the tube formation according to bright images. Then, EPCs were stained with calcein-AM at 37 °C for 15 min. Fluorescent images of each well were acquired under the inverted fluorescence microscope (Ti2-A, Nikon, Japan).

2.9. Transwell migration assay

G_5H_2 composite hydrogels containing 50ug USC^{EXO} s were Placed on the transwell plate's bottom layer, adding the medium containing 10% serum and cells planted in the upper layer of the chamber adding the medium containing 5% serum. Then, transwell plates were incubated at 37 °C for 12 h, followed by staining with 4% crystal violet reagent before water cleaning 3 times with double-distilled water. Finally, the observation was performed under the inverted light microscope (Ti2-A, Nikon, Japan) and analyzed statistically using ImageJ software.

2.10. Gene expression analysis

A NanoDrop-2000 spectrophotometer (Thermo Fisher Scientific) was used to measure the concentration of RNA, when the BMSCs and composite hydrogels in the well plates were incubated for 14 days and the EPCs were incubated for 1 day. Subsequently, cDNA was synthesized using the Premix RT Evo M-MLV kit. Finally, qRT-PCR was performed using the SYBR Green Premix Pro Taq HS kit. Three parallel specimens were prepared for each group. The Ct ($2^{-\Delta\Delta\text{Ct}}$) comparison method was used to determine the relative expression. Primer sequences, including GAPDH, Runt-related transcription factor 2 (RUNX-2), bone morphogenetic protein (BMP-2), and osteocalcin (OCN), platelet endothelial cell adhesion molecule-1 (CD31), hypoxia-inducible factor-1 alpha (HIF1A), and fibroblast growth factor-1 (FGF1), were listed in Table 2.

2.11. Animals

All animal experiments were approved by the Department of Laboratory Animal Management, Central South University (No.2020sydw0972). All Sprague–Dawley (SD) rats (200–250 g, 8 weeks) were purchased from Hunan SJA Laboratory Animal Company (Changsha, China).

To track the retention of exosomes, labelled by DiR green, fluorescent reagent, in the organism. The statistics ($n = 3$) were analyzed for fluorescence intensity at various times using a live imaging system (FMT-4000; PerkinElmer, USA). To verify the biocompatibility of the hydrogels

Table 2
Primers used for RT-qPCR.

Gene name	Forward primer sequence (5'-3')	Reverse primer sequence (3'-5')
GAPDH	CAGGCTGCTTTTAACTCTGG	TGGGTGGAATCATATTGGAACA
BMP-2	ACTACCAGAAACGAGTGGGAA	GCATCTGTCTCGGAAAACCT
Runx-2	TCTTCCCAAAGCCAGAGCG	TGCCATTGAGGTGGTCG
OCN	CACCTCTCGCCCTATTGGC	CCCTCTGCTTGGACACAAAG
CD31	CACCGTGATACTGAACAGCAA	GTCACAATCCCACCTTCTGTG
HIF1A	GGGTTATGAGCCAGAAAGAACT	CCTGTGGTGACTTGTCCCTTA
FGF1	TTCTCAGGGTGTCTAAGCTGC	GGGGATCAGTTGGGTTCTTGT

in vivo, the sub-skin embedded hydrogels were, at various times, assembled to do H&E staining and to observe the morphology of the hydrogels and the inflammatory reaction involving the periphery under the inverted light microscope (Ti2-A, Nikon, Japan). The results were processed using ImageJ software. For the rat cranial bone defect model after the surgery for 4 weeks, the rats were sacrificed, and all samples were fixed with 4% paraformaldehyde before being scanned for imaging evaluation using a micro-CT imaging system (SkyScan 1176; SkyScan, Aartselaar, Belgium). Then, a cylindrical region of interest (Φ 4 mm \times 2 mm) was established to calculate the new bone volume relative to the total volume (BV/TV), trabecular number (Tb. N), trabecular thickness (Tb. Th) and trabecular separation (Tb. Sp). Finally, 3D reconstruction was performed with Mimics v10.01 software (Materialise, Leuven, Belgium).

2.12. Histological and immunofluorescence staining analysis

Samples were then submerged in 10% EDTA solution for 3 weeks for decalcification, embedded in paraffin, and prepared into 5 μ m sections, followed by H&E staining and Masson's trichrome staining to assess regenerated bone and collagen fibers. Subsequently, RUNX-2 and OCN, osteogenic-associated proteins, were stained by immunohistochemistry (IHC) and immunofluorescence (IF) assays, respectively. In addition, the angiogenic-associated proteins CD31 and EMCN were stained by immunofluorescent staining. After observing the stained sections, a multispectral tissue scanner (Panoramic midi, 3D HISTECH) was used, and the sections were analyzed by Case Viewer software.

2.13. Statistics analysis

All data were analyzed using GraphPad 8.0 statistical software. One-way or two-way analysis of variance (ANOVA) was used to compare experimental data among groups. Data were considered statistically significant at $p < 0.05$.

3. Result

3.1. The physicochemical structure of composite hydrogels

The ingredients employed in the synthesized hydrogels include nHAP, GelMA and HAMA, which render the inks liquid flowable prior to photocrosslinking (Fig. 1A). The hydrogels showed injectable properties and fabricated different shapes under photocrosslinking conditions by adjusting the composition ratios (Fig. 1B).

The results of SEM show that the porous structure exists in composite hydrogels with different HAMA constitution proportions, with the pore size within 300 μ m, certifying the existence of internal connecting pores in composite hydrogels (Fig. 1C).

Subsequently, we used ^1H NMR spectroscopy to confirm whether GelMA-HAMA was successfully synthesized and retained the methacrylate-functional molecules. In the methacrylate group, double bond peaks were observed at 5.38 ppm and 5.61 ppm, while chemical shift peaks were also observed at 5.7 ppm and 6.13 ppm, which are in agreement with ^1H NMR spectra of GelMA and HAMA, respectively as shown in Fig. 1D. These chemical shift peaks confirm that $-\text{CH}=\text{CH}-\text{CH}_3$ or $-\text{CH}=\text{CH}_2$ groups were successfully grafted onto the products [29,31].

The FTIR spectra of the composite hydrogels exhibit bands for polymer components. The maximum values of the amide bond and CH stretching vibrations are similar to the pure GelMA positions, at 1630, and 1584 cm^{-1} , respectively, which is consistent with the expected results, due to the predominance of GelMA in the selected hydrogel composition. Furthermore, in-plane vibrations corresponding to the C–N and N–H groups of the bound amide, vibrations of the CH_2 group of the amino-glycine and skeletal stretching at 1540, 1238, and 1067 cm^{-1} , respectively, indicate intermolecular interactions between GelMA and HAMA chains during the gel formation of the hybrid hydrogel. In

addition, electrostatic interactions were generated between the hydrogen bonds in the hydrogen-rich portions of the two polymer chains and between the amino group of the lysine of GelMA and the HAMA carboxyl group, which may enhance the mechanical strength when the mutual cross-bonding [22,32].

3.2. The multifunctional properties of composite hydrogels

As demonstrated by rheological results (Fig. 2A and B), GelMA-HAMA/nHAP inks prepared in various proportions are a non-Newtonian fluid tending to solid-stability (storage modulus $G' >$ depletion modulus G''). The results from the strain sweeps (0.01–1000% strain; 10 rad s^{-1}) revealed that the compression strength (G') was enhanced with the increasing HAMA ratio. Otherwise, the results from frequency sweep measurements (0.01–100 rad s^{-1} ; 1% strain) implied that the curves of G' and G'' have no tendency to converge, which possesses a stable condition inside inks irrespective of the angular frequency. As the results of kinetic viscosity (0.1–1000 s^{-1}) and the temperature sweep (1 s^{-1} , 10–40 $^\circ\text{C}$) are shown in Fig. 2D and E, the increasing percentage of HAMA can enhance the viscosity of the ink at room temperature. No significant difference in the viscosity of the inks. However, changed when the environmental temperature varied from 30 $^\circ$ to 40 $^\circ$.

Based on the stress-strain curve results related to photocrosslinked hydrogels (Fig. 2C), adding HAMA can modify the hydrogel's compressive strength. Also, compressive strength at 40% ultimate strain was calculated from the curve (Fig. 2F). The compressive modulus of the hydrogels was 8.4 \pm 0.6 kPa, 12.2 \pm 0.7 kPa, and 21.1 \pm 1.6 kPa, corresponding to 1, 1.5, and 2 wt% of HAMA incorporation, respectively. The swelling behavior of the hydrogels is shown in Fig. 2G. From the 12th hour onwards, the swelling of hydrogels in various groups tends to become stable. Nevertheless, there was no significant difference in swelling values among the groups. The kinetic release behavior of the hydrogels is shown in Fig. 2H. The exosomes released from the fluorescently labelled hydrogels in each group remained detectable on day 17. Notably, the values of kinetic release were also not significantly different among the groups.

3.3. The characterization of exosomes

The TEM results were shown in Fig. S2A. The exosomes were in oval spheres with a membrane structure. The NTA results indicated that the diameter of the majority of exosomes ranged from approximately 50 μm –200 μm (Fig. S2B). Western blotting results showed that the Calnexin (endoplasmic reticulum secretory protein) was expressed in USC, whereas CD63 and TSG101 (exosome-specific markers) were expressed in $^{\text{USC}}$ EXOS. Characterization of the secretions extracted from urine-derived stem cells (Fig. S2C).

3.4. The cell biocompatibility, migrations and exosomes internalization of $^{\text{USC}}$ EXOS/ G_5H_2

To assess the biocompatibility of the hydrogels. The hydrogels containing various HAMA ratios were co-cultured with BMSCs and EPCs. After one day of co-culture, the cells were treated with live-dead staining assays and observed under a confocal laser scanning microscope (live cells labelled with green fluorescence, dead cells labelled with red fluorescence). The results demonstrated that the hydrogels were not significantly cytotoxic (Fig. 3A and Fig. 4A). Meanwhile, the effect of hydrogels on cell viability was investigated by the CCK8 method on day 1, day 2, and day 3 of co-culture, respectively. Results showed no statistical difference between the groups of hydrogels on the viability of BMSCs and EPCs (Figs. 3B and 4B).

To verify whether urine stem cell-derived exosomes can be phagocytosed by target cells, BMSCs and EPCs were co-cultured with DiI-labelled exosomes (fluorescently labelled in red) for 12 h, respectively.

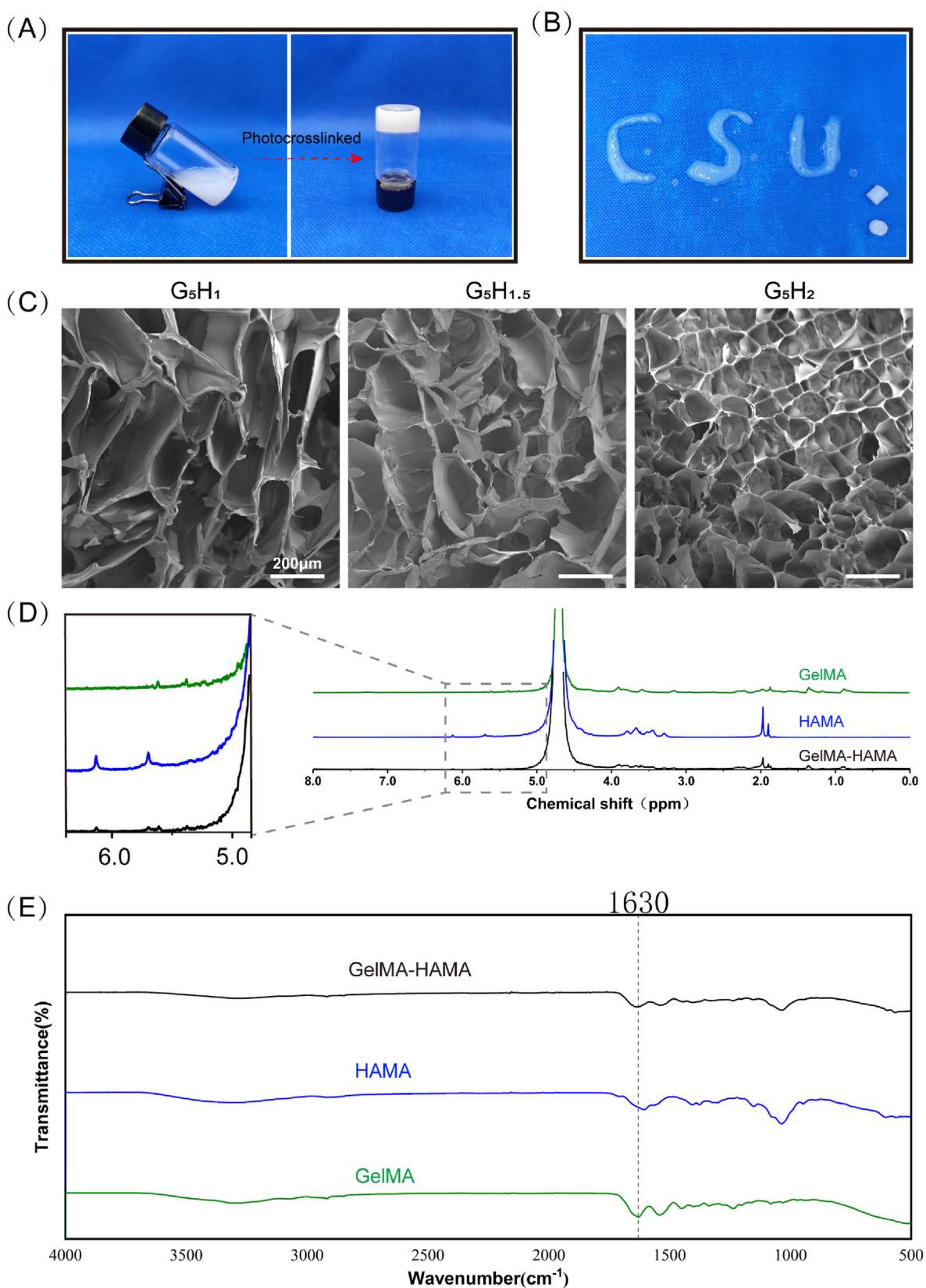


Fig. 1. Physicochemical properties of GelMA-HAMA photocrosslinkable hydrogels. (A) Fluidable composite bioink transformed into concrete hydrogel via photocrosslinking. (B) The injectable composite hydrogel demonstrates the ability to vary the shape of the material. (C) The composite hydrogel possesses a sparse, porous structure observed by SEM after Lyophilization treatment. (D) The ^1H NMR of composite hydrogels. (E) The FTIR of composite hydrogels.

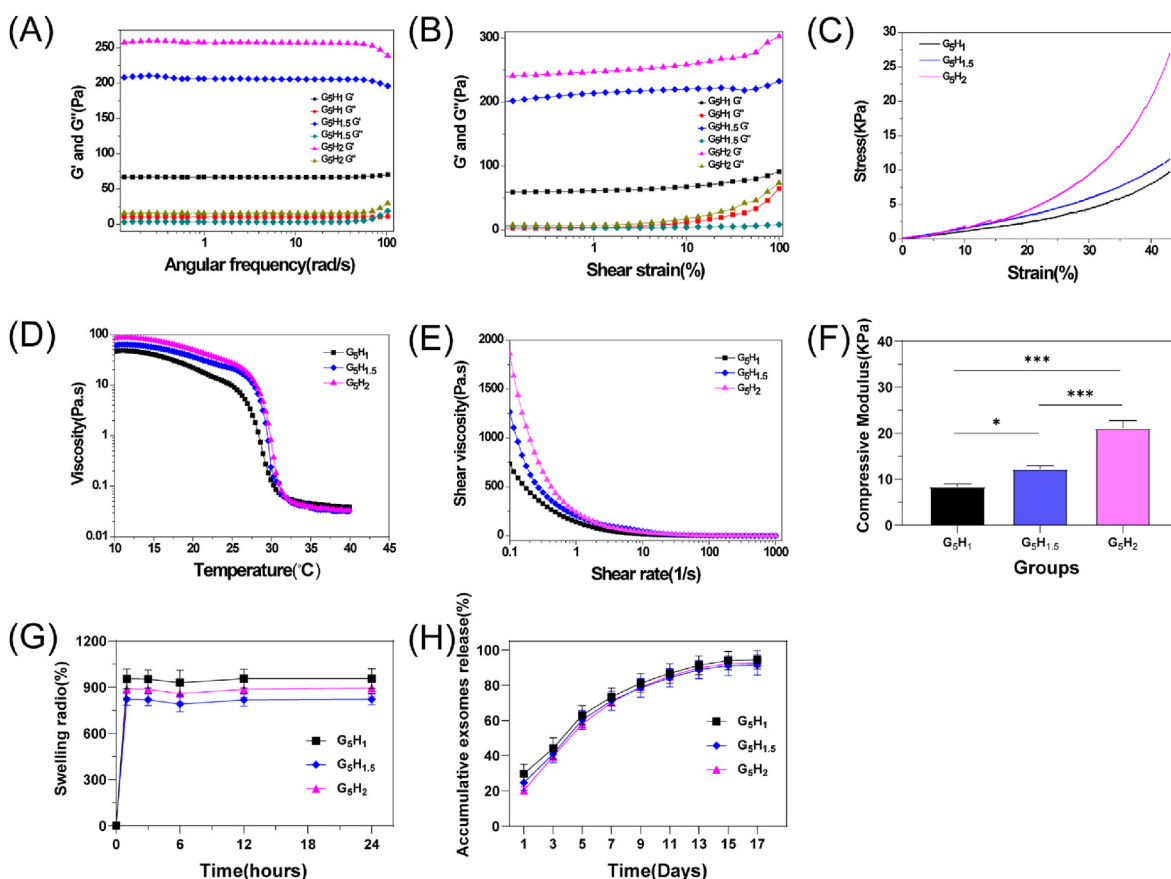


Fig. 2. Characterization of the composite hydrogels. (A), (B), (D) and (E) Rheological and mechanical properties of composite hydrogels with a variety of HAMA compositions. (C) Compressive stress-strain curve of the composite hydrogel. (F) The ultimate compressive modulus of the composite hydrogel when the strain reached 40%. (G) The swelling properties of composite hydrogels. (H) Composite hydrogels with different HAMA ratios demonstrate the retardation property of exosome release in vitro. Data are shown as mean \pm standard error ($n = 3$). (* $p < 0.05$, ** $p < 0.01$, *** $p < 0.001$.)

Our results demonstrate the ability of exosomes in cell existence by confocal laser scanning microscopy (Figs. 3C and 4C).

Transwell chambers were stained with crystal violet reagent, allowing BMSCs and EPCs migrating to the bottom of chambers through pores to be visible under the inverted light microscope (Figs. 3F and 4F). Besides, the semi-quantitative results according to Figs. 3I and 4M demonstrate that the G₅H₂ hydrogels containing exosomes possess.

3.5. Promotion of osteogenesis with BMSCs

To confirm the osteogenic ability of G₅H₂ composite hydrogels containing ^{USC}EXOs, the composite hydrogels were co-cultured with BMSCs. Alizarin Red staining on day 14 exhibited significantly more stained areas in the ^{USC}EXOs/G₅H₂ composite hydrogels than in the blank group (Fig. 3D and G) and was statistically different ($p < 0.01$). Nevertheless, it was not significantly higher than the control group ($p > 0.05$).

Meanwhile, the Alkaline Phosphatase staining results on day 3 showed that osteoblasts were observed in all groups, as well as the ability of ^{USC}EXOs/G₅H₂ composite hydrogel to induce osteogenesis was more robust than the other groups (Fig. 3E and H), which was statistically significant ($p < 0.05$).

More importantly, the 14-day qPCR results also confirmed (Fig. 3J-L) that osteogenesis-related proteins BMP-2, RUNX-2, and OCN were expressed in the ^{USC}EXOs/G₅H₂ composite hydrogel group than the other groups ($p < 0.05$), which was consistent with the results of osteogenesis-related staining.

3.6. Promotion of angiogenesis with EPCs

For tube formation assay in vitro, we recorded the images of tubes formed by EPCs under the inverted light microscope after 5 h and the inverted fluorescence microscope after 6 h, respectively (Fig. 4D and E). Total Length, Number of Junctions, and Number of Branches were recorded and analyzed by analytical software. Statistical results revealed that ^{USC}EXOs/G₅H₂ composite hydrogel could effectively promote tube formation (Fig. 4G-I, $p < 0.001$).

In addition, CD31, HIF1A, and FGF1, associated with angiogenesis, were significantly more expressed in the ^{USC}EXOs/G₅H₂ composite hydrogel group than in the other groups (Fig. 4J-L, $p < 0.001$).

3.7. ^{USC}EXOs/G₅H₂ enhances USC exosomes retention in vivo

In our initial experiments in vivo, we verified the ability of the composite hydrogel to retain urine-derived stem cell exosomes subcutaneously in the rat skull (Fig. 5B). Both the exosomes loaded in the composite hydrogel and the exosomes diluted in PBS solution were retained in vivo for several days in Fig. 5A. Further statistical data analysis showed that the composite hydrogels were able to enormously enhance the retention of exosomes in vivo according to Fig. 5C ($p < 0.05$ and $p < 0.001$, respectively). The above demonstrated that the photocrosslinked composite hydrogels based on methacrylated gelatin and methacrylated hyaluronic acid possess excellent retention of the incorporated exosomes.

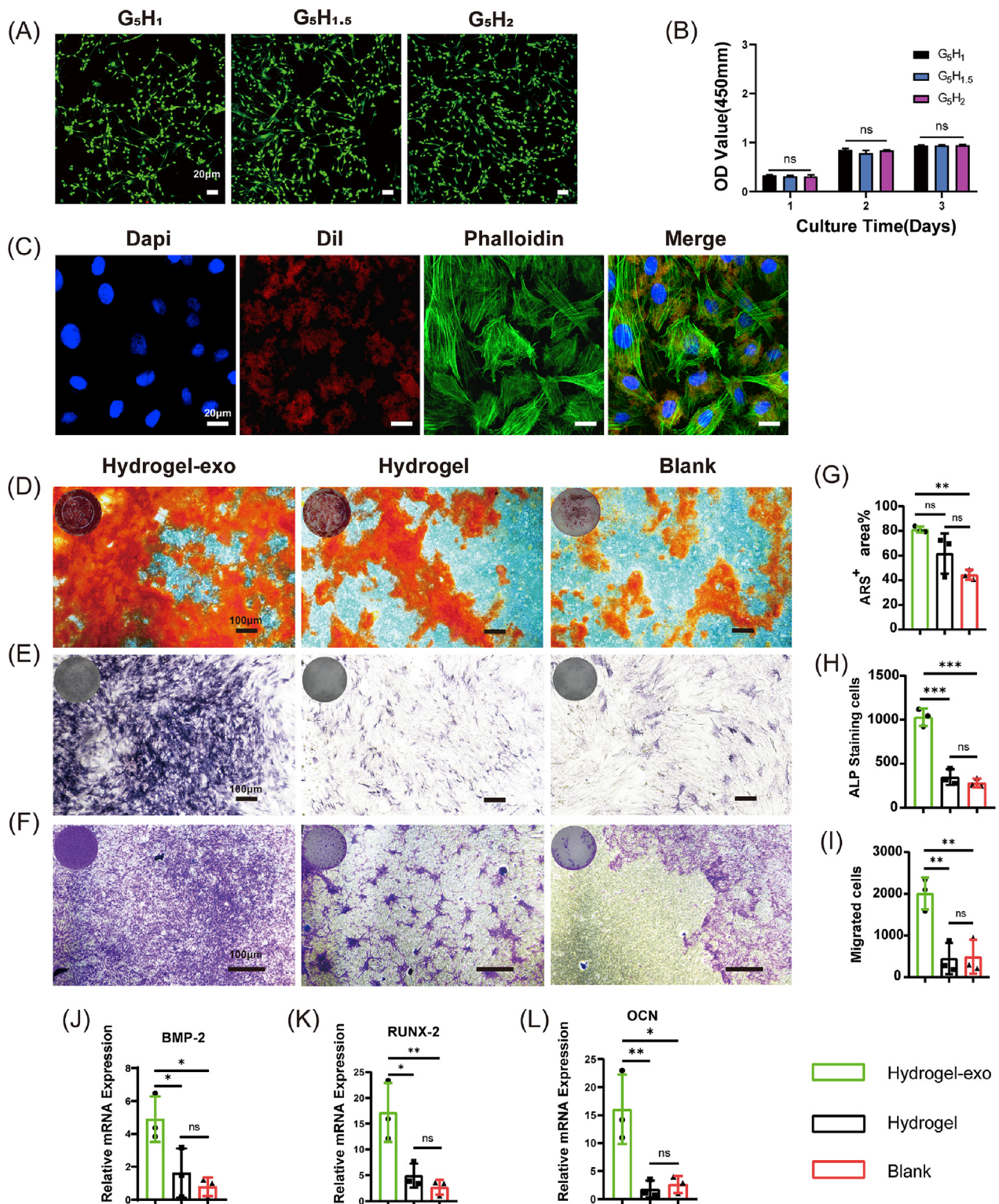


Fig. 3. Osteogenic properties of composite hydrogel-loaded human urine-derived stem cell exosomes in vitro. (A) Live/dead assay and (B) CCK8 assay demonstrate the biocompatibility of composite hydrogels with various HAMA ratios co-cultured with BMSCs. (C) Fluorescently labelled exosomes can be internalized by BMSCs, observed by laser confocal scanning microscopy. (D) Alizarin red staining and (G) semi-quantitative results in co-culture for 14 days. (E) Alkaline phosphatase staining and (H) semi-quantitative results in co-culture for 3 days. (F) Crystalline violet staining and (I) semi-quantitative results of Transwell chambers in co-culture for 12 h. (J–L) Real-time fluorescence quantitative polymerase chain reaction to detect the expression level of osteogenesis-related genes in co-culture for 14 days. Data are shown as mean ± standard error (n = 3). (*p < 0.05, **p < 0.01, ***p < 0.001). (For interpretation of the references to colour in this figure legend, the reader is referred to the Web version of this article.)

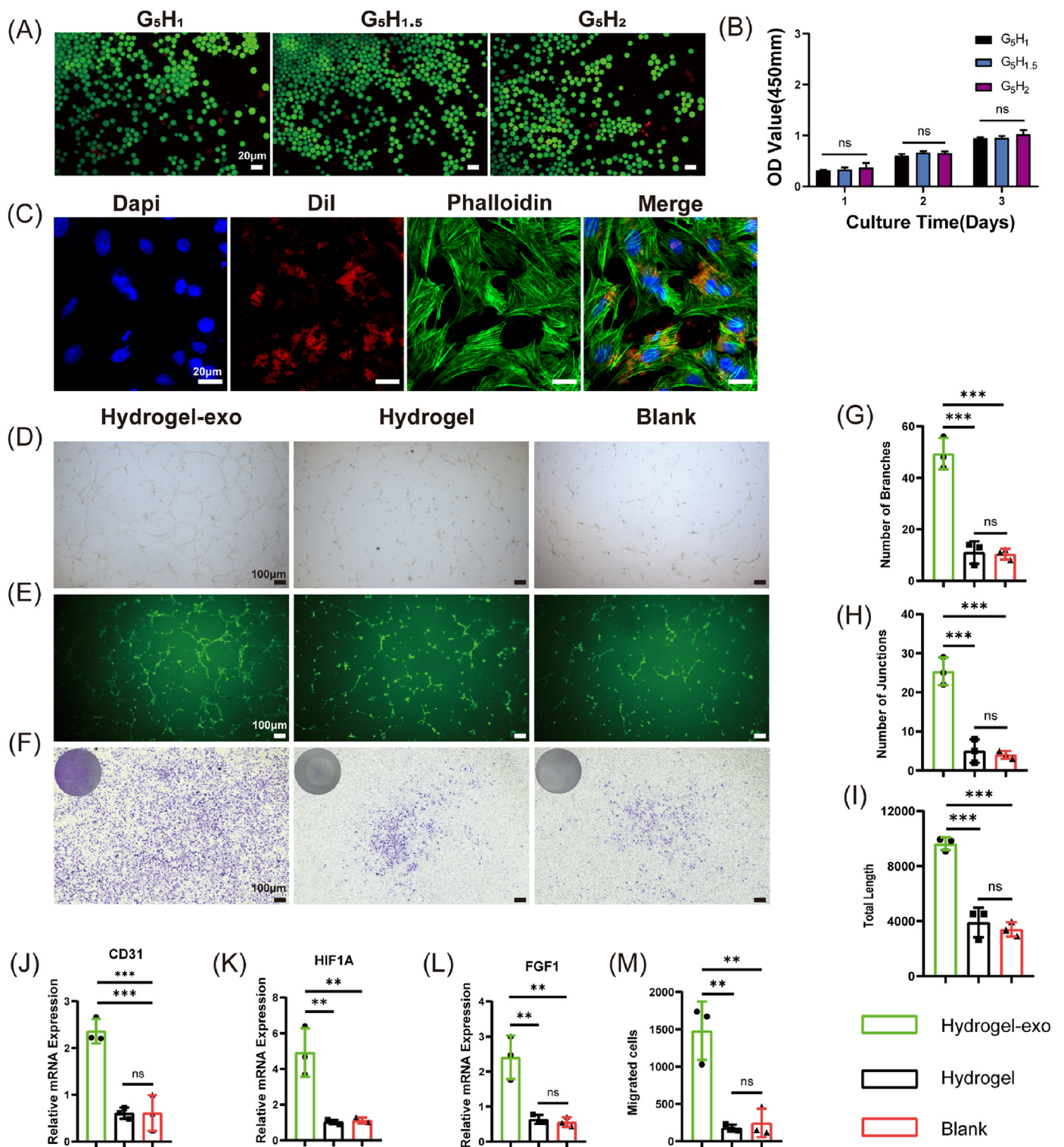


Fig. 4. Angiogenic properties of composite hydrogel-loaded human urine-derived stem cell exosomes in vitro. (A) Live/dead assay and (B) CCK8 assay demonstrate the biocompatibility of composite hydrogels with various HAMA ratios co-cultured with EPCs. (C) Fluorescently labelled exosomes can be internalized by EPCs, observed by laser confocal scanning microscopy. (D) Observation of tube formation under the inverted light microscopy in co-culture for 5 h and (E) Observation of tube formation under the inverted fluorescence microscopy in co-culture for 6 h. (G–I) Semi-quantitative results of tube formation assays. (F) Crystalline violet staining and (M) semi-quantitative results of Transwell chambers in co-culture for 12 h. (J–L) Real-time fluorescence quantitative polymerase chain reaction to detect the expression level of angiogenesis-related genes in co-culture for 1 day. Data are shown as mean \pm standard error ($n = 3$). (* $p < 0.05$, ** $p < 0.01$, *** $p < 0.001$). (For interpretation of the references to colour in this figure legend, the reader is referred to the Web version of this article.)

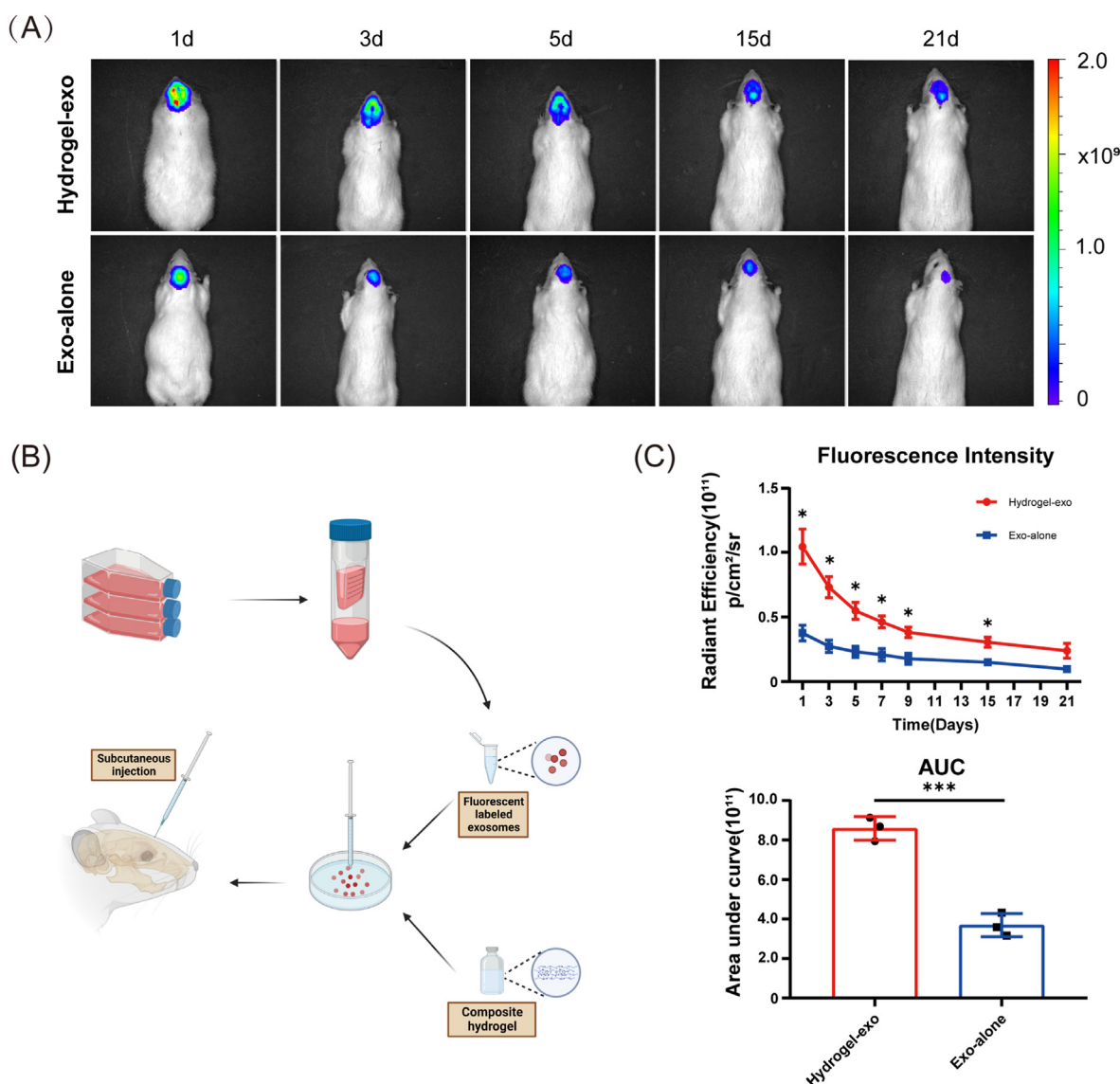


Fig. 5. Subcutaneous injection of G₅H₂ composite hydrogel loaded with human urine-derived stem cell exosomes in rat cranium to establish an in vivo time-release exosomes model. (A) Fluorescence imaging of fluorescently labelled human urine-derived stem cell exosomes in rat cranium over time. (B) Procedures for sustained release of exosomes in vivo. (C) Fluorescence intensity of retained fluorescently labelled exosomes in vivo with time. Data are shown as mean \pm standard error ($n = 3$). (* $p < 0.05$, ** $p < 0.01$, *** $p < 0.001$.)

3.8. The biocompatibility of composite hydrogels in vivo

To verify the biocompatibility of the composite hydrogels in vivo, we employed a rat model in which composite hydrogels containing different HAMA components were subcutaneously embedded in the back (Fig. S1B). The hydrogels, collected at different time points, were subjected to H&E staining, and the morphology was observed under the inverted light microscope. Notably, the hydrogels were homogeneous without macrophage distribution. However, with a tendency that its internal morphology gradually collapsed and degraded over time, while the higher the HAMA composition the slower the rate of internal collapse of the hydrogel (Fig. S1A). In the case of the hydrogels, we also analyzed the fibrous capsule thickness around the hydrogels, which showed no statistically significant difference between the data, as shown in Fig. S1C.

3.9. *USC* EXOs/G₅H₂ promotes cranial bone defects regeneration in vivo

Cranial bone defect regeneration was evaluated using a rat model, in which 3D reconstruction and coronal images were obtained and analyzed

through micro-CT (Fig. 6A). The analyzed results of Micro-CT are shown in Fig. 6B. The bone volume/tissue volume (BV/TV) of regenerated bone tissue in the Exo-alone group was $23.3 \pm 5.9\%$, which was significantly high compared to the Hydrogel and Blank groups, corresponding to $12 \pm 6\%$ and $7.6 \pm 6\%$, respectively. Nevertheless, the value of the Hydrogel-exo group ($32.5 \pm 6.4\%$) was highest compared to the other groups. In addition, for regenerated bone tissue in the defective bone cavity, Trabecular number ($1.4 \pm 0.3 \text{ mm}^{-1}$), Trabecular thickness ($0.4 \pm 0.1 \text{ mm}$) was higher in the Hydrogel-exo group than in the other groups, and Trabecular separation ($0.3 \pm 0.1 \text{ mm}$) reversed. The implication was that the Hydrogel-exo group had an osteogenesis facilitative effect.

Subsequently, harvested regenerated bone tissue was assessed by H&E and Masson's trichrome staining. The results of H&E staining showed that a remarkable amount of new bone in the hydrogel-exo group occurred in the defect area and integrated considerably with the host bone. Regenerating bone cavities, and central canals were observed inside the new bone tissue. Moreover, the hydrogel implanted was degrading for a while. The regenerated bone in the Exo-alone group was

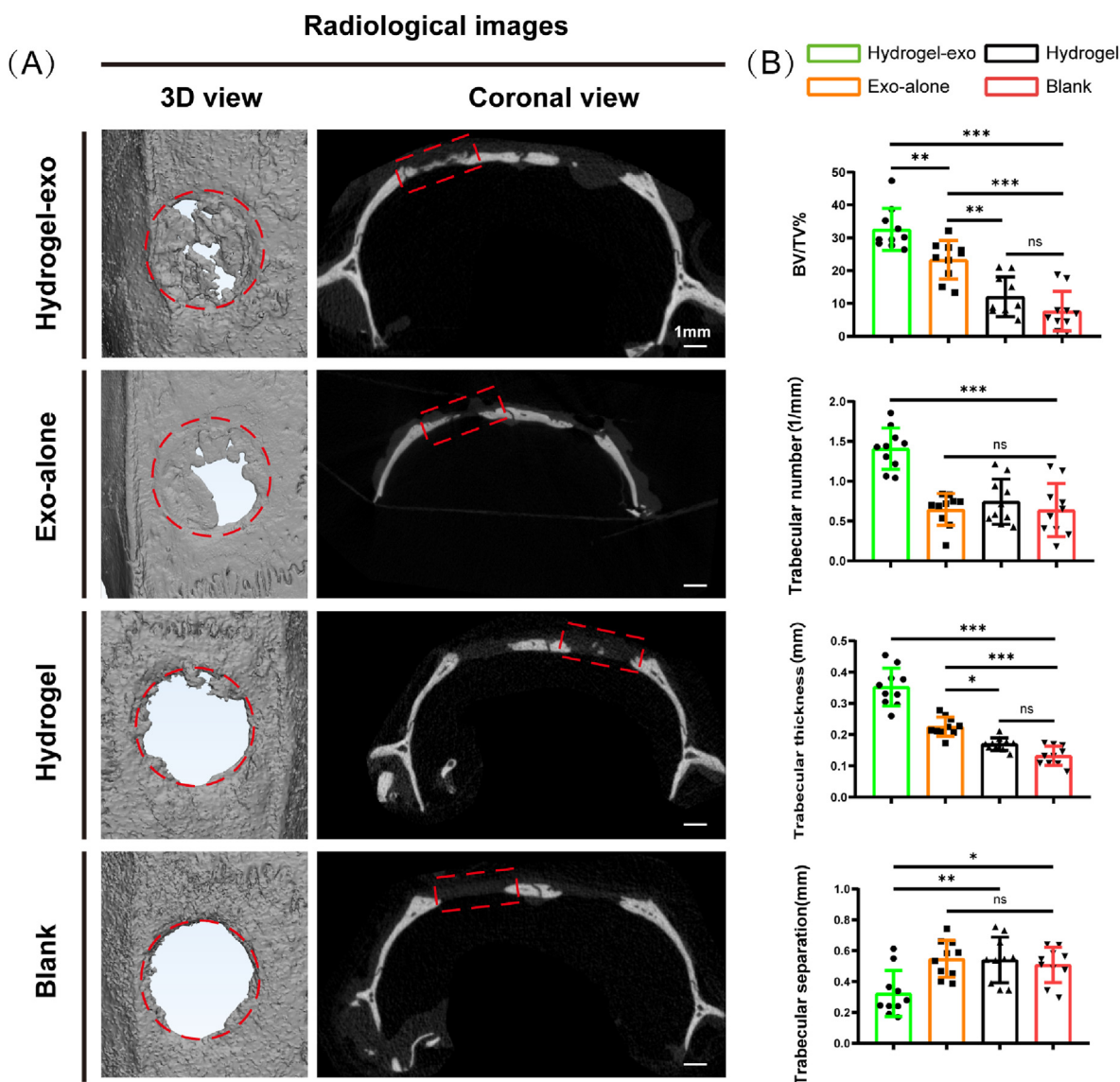


Fig. 6. Results of Micro-CT analysis of rat cranial bone defect model at week 4. (A) 3D view and coronal imaging were shown in different groups. (B) Quantitative results of Micro-CT analysis concerning different groups. Data are shown as mean \pm standard error ($n = 10$). (* $p < 0.05$, ** $p < 0.01$, *** $p < 0.001$.)

poorly integrated with the surrounding host bone, and its regenerated bone morphology was less well-developed than the Hydrogel-exo group. Nevertheless, rarely newly formed bone was present in Hydrogel and Blank groups (Fig. 7A). By Masson's trichrome staining, it was observed that few collagen fibres formed in regions with bone defects which were present in the Hydrogel and Blank groups. Nonetheless, there was collagen formation in regions with bone defects in the Hydrogel-exo and Exo-alone groups, the former with mature collagen fibres (red) and the latter with relatively immature collagen fibres (blue) (Fig. 7B).

As RUNX-2 immunohistochemistry results illustrate, the positive regions in the Hydrogel-exo and Exo-alone groups were significantly higher than in other groups. The former had the highest values (Fig. 8A and Fig. 8D). Immunofluorescence results suggest a high expression of osteogenic-related protein OCN in the Hydrogel-exo group compared to other groups (Fig. 8B and E). Interestingly, we identified that the coupling-associated osteogenic-angiogenic H-type vessels were abundantly expressed in the Hydrogel-exo group (Fig. 8C and F). It demonstrated excellent osteogenesis. These findings are consistent with the micro-CT scan analysis and histological staining, reinforcing our synthesized composite hydrogel's superior osteogenic and angiogenic capabilities.

4. Discussions

In the present experiment, we developed a novel hydrogel that can instantaneously fill various regions under photocrosslinking conditions. Loaded with human ^{USC}EXOs, we verified that the composite hydrogel could accelerate the osteogenic process, mediated by coupling into angiogenesis. The Microporosity structure of composite hydrogel and its internal nHAP were confirmed by SEM. The mechanical properties of pure GelMA hydrogels were less than ideal. Combined with the introduction of photocross-linked HAMA hydrogels and ultrasonically emulsified nHAP, the mechanical properties of the composite hydrogels were significantly reinforced. Besides, the hydrogen proton ¹H NMR spectra of the composite hydrogels demonstrated that the methacrylated gelatin and hyaluronic acid methacrylate successfully photocrosslinked with each other and simultaneously retained $-\text{CH}=\text{CH}-\text{CH}_3$ or $-\text{CH}=\text{CH}_2$ functional groups, which is consistent with the published literature [29, 33,34]. The physiological roles of ^{USC}EXOs implicated in osteogenesis, angiogenesis, and anti-inflammation have been demonstrated [11,35]. ^{USC}EXOs fluorescence retardation experiments demonstrated that the composite hydrogel possesses superior exosomes retention properties via in vitro and in vivo experiments. Furthermore, it was shown that

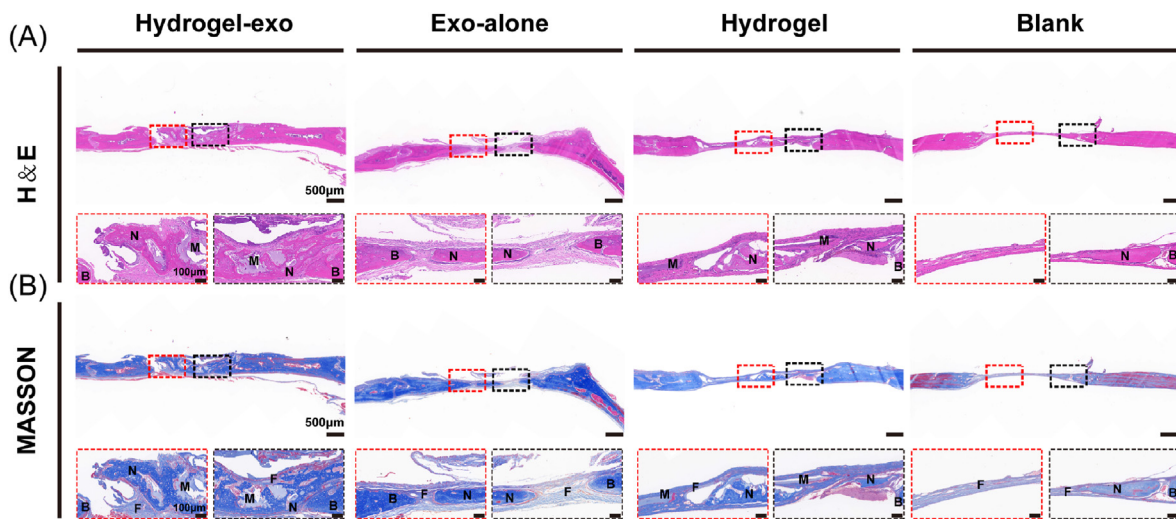


Fig. 7. H & E staining and Masson's trichrome staining results of rat cranial bone defect model. (A) H & E staining of regenerated bone tissue was observed in different groups at 4 weeks after the surgery. (B) Masson's trichrome staining was observed in different groups at 4 weeks after surgery. (N: new bone tissue. M: material. F: fibrous tissue. B: old bone border).

composite hydrogels loaded with ^{USC}EXOs can promote osteogenesis and angiogenesis in vitro experiments. Intriguingly, composite hydrogels loaded with ^{USC}EXOs promote the generation of H-type vessels, resulting in coupled osteogenic-angiogenic processes through a rat model of cranial bone defects.

Gelatin, as a protein-based polymer, is a collagen partially degraded peptide containing an arginine-glycine-aspartate sequence, which can interact directly with cell surface integrins to promote cell adhesion [36–38]. It is more attractive as a precursor for hydrogels preparation due to its processability, superior water solubility, and lower immunogenicity compared to collagen [39–41]. Nonetheless, pure gelatin has a faster degradation rate and poorer mechanical properties, often falling short of expectations [42]. Hyaluronic acid (HA), a polysaccharide-based polymer consisting of a disaccharide unit composed of glucuronic acid and N-acetyl glucosamine, exists in soft tissue and synovial fluid, interacts with the extracellular matrix of cartilage and plays an essential role in mesenchymal cell migration, cohesion, cartilage differentiation and maintenance of intrachondral homeostasis [43–45]. HA, in particular, promotes wound healing, tissue regeneration, and osteoblasts formation. In addition, HA has been approved by the U.S. Food and Drug Administration for human implantation due to its nontoxic nature and natural mammalian existence [46]. Specifically, the dense internal structure of HA allows it to maintain superior mechanical properties and a slow degradation rate [47,48].

To gelatinize the injectable hydrogels, we employed GelMA and HAMA to facilitate the formation of hydrogels with three dimensions in temporal and spatial terms subject to blue light irradiation conditions (405 nm). In addition, we introduced nHAP into the composite hydrogel aiming to strengthen the mechanical properties of the composite hydrogel. Liu et al. reported that the preparation of GelMA-HAMA-based hybrid hydrogels showed favourable mechanical properties and successful drug loading [29]. Yang et al. worked on biomimetic mineralization using bioinks such as GelMA and HAMA as the basis for 3D bioprinting successful [49]. In our assay, the novel composite hydrogel we prepared possesses remarkable rheological properties and compressive modulus, demonstrating that the composite hydrogel can maintain liquid fluidity before photocrosslinking and solid-state stability after photocrosslinking, providing an excellent three-dimensional loading network for subsequent experiments. However, the degradation rate of our prepared composite hydrogels was slow in vitro, and we will further exploit the composite hydrogel components and optimize the fabrication method.

As an important membrane-bound carrier in extracellular vesicles, exosomes have been increasingly investigated in recent decades. Exosomes are endosome-derived membrane-bound vesicles with diameters between 50 and 150 nm and are released by various cells in all living organisms under physiological and pathological conditions, mediating intercellular communication via their inclusions (proteins, nucleic acids, and lipids) [50,51]. Sutherland et al. were the first to report successful culture of exfoliated cells from human urine [52]. Rahmoune et al. demonstrated that most of these cells originate from the renal epithelium, but also from the uroepithelium [5]. Further, a subpopulation of urothelial cells was identified that expressed stem cell markers and had multifunctional differentiation potential [35,53]. Our group successfully demonstrated in the previous study that ^{USC}EXOs have the physiological function of promoting osteogenesis and inhibiting osteolysis [10,11]. Nevertheless, the poor retention of ^{USC}EXOs in vivo may restrict other biological effects and clinical promotion. In this study, we innovatively loaded ^{USC}EXOs into a GelMA-based composite hydrogel, which provided superior temporal and spatial release properties for exosomes. We demonstrated that a composite hydrogel loaded with ^{USC}EXOs effectively promoted the osteogenic capacity of BMSCs and the angiogenic capacity of EPCs in vitro. The regenerated bone tissue in rats' cranial bone defect region was also significantly increased. In addition, we demonstrated that our new composite hydrogel could effectively boost the retardation effect of exosomes, enhancing osteogenesis and angiogenesis in vitro and in vivo.

Bone regeneration involves the formation of an abundant vasculature, which is related to bone formation during skeletal development and intimately related bone remodelling, termed osteogenic-angiogenic coupling [54,55]. Blood vessels are responsible for providing essential oxygen, nutrients, and growth factors to bone tissue, and recent research has identified new vascular subtypes that play an essential role in the regulation of bone formation. Some researches characterized the capillary subtype as having high expression of CD31 and Endomucin (CD31^{hi}EMCN^{hi}) as a type H vessel associated with osteogenesis [56,57]. H-type vessels are densely surrounded by bone progenitor cells expressing Osterix and RUNX-2 transcription factors, both of which contribute to the efficient formation of bone [58]. Zhai et al. studied the vascular discrepancy and osteogenic effectiveness associated with the specification of H-type vessels in healing and non-healing cranial bone defects through high-resolution multiphoton laser scanning microscopy, which suggests that the bone tissue-specific H-type vascular specification may play an essential role in bone regeneration [59]. Kusumbe et al.

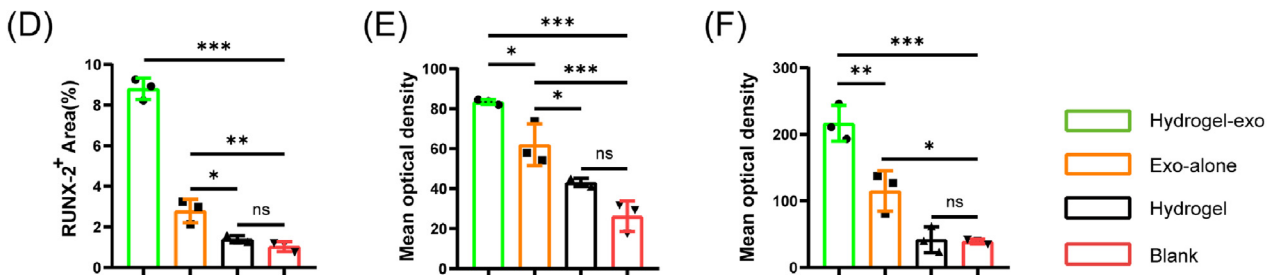
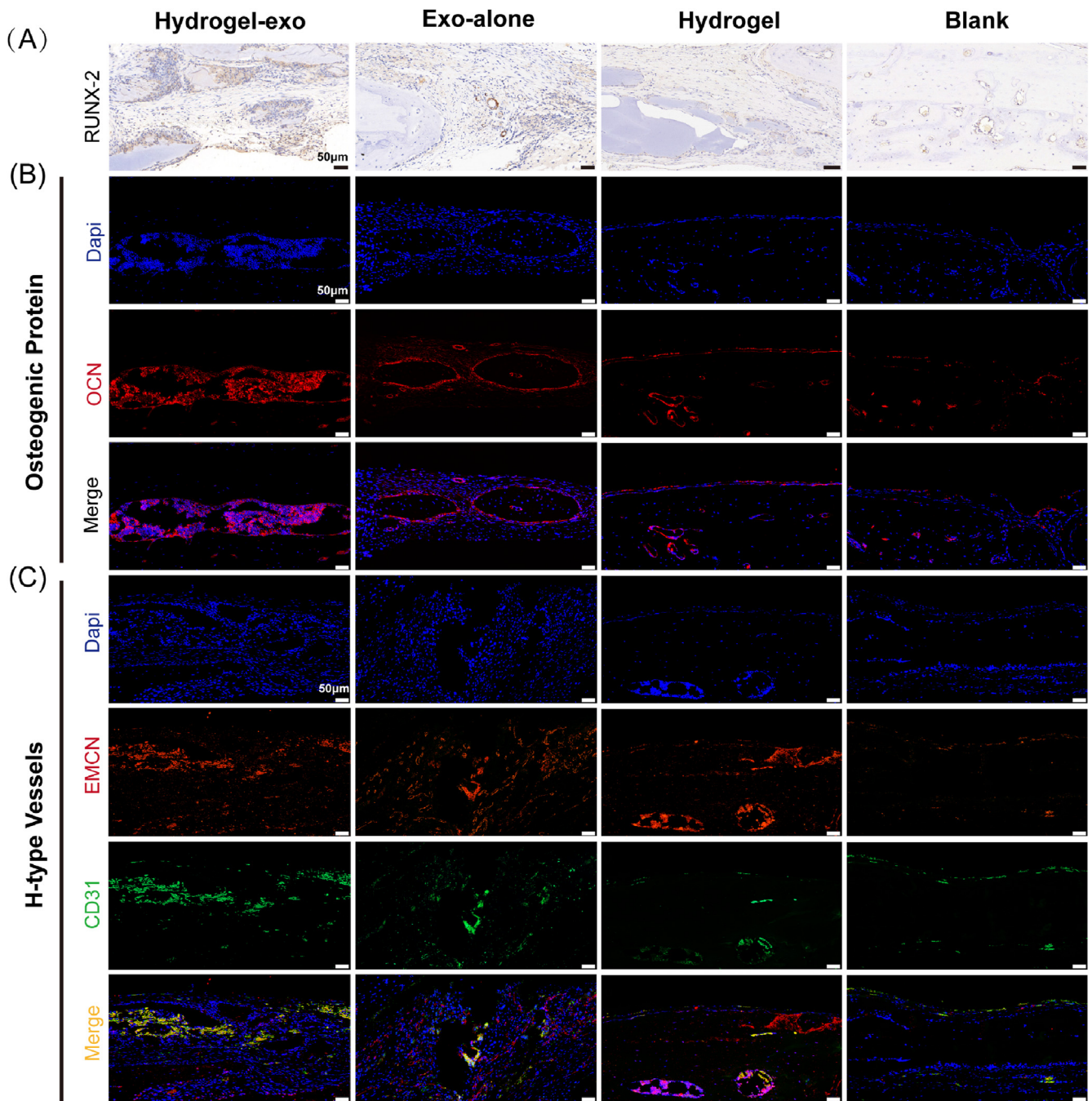


Fig. 8. Histological staining results of osteogenic-associated and angiogenic-associated proteins in a rat cranial bone defect model. (A) Immunohistochemical staining of RUNX-2 (B) Immunofluorescence staining of OCN (C) Immunofluorescence staining of H-type Vessels related proteins. (D) Semi-quantitative results of the osteogenesis-related protein RUNX-2. (E) Semi-quantitative results of osteogenesis-related protein OCN. (F) Semi-quantitative results of H-type Vessels related proteins. Data are shown as mean \pm standard error (n = 3). (* p < 0.05, ** p < 0.01, *** p < 0.001).

found that H-type endothelial cells constituted no more than 2% of the endothelium, but intriguingly, more than 82% of RUNX-2⁺ and more than 70% of Osterix⁺ osteoprogenitor cells were selectively located around H-type endothelial cells [60]. In our present experimental study, we can confirm from the immunohistochemical results of cranial bone regeneration that RUNX-2 was strongly expressed in the composite hydrogel group loaded with USC-EXOs and the immunofluorescence results of CD31^{hi}EMCN^{hi} were significantly higher than the rest of the groups. This is consistent with the published literature. HIF1 was identified as a transcriptional activator of erythropoietin, as a central molecule in the mechanism of oxygen adaptation [61,62]. In hypoxic or blood-deficient cells, HIF1A is one of the main isoforms that induce VEGF expression, which is responsible for markedly expanding endothelial cells and epiphyseal vascular columns of type H concomitant with increased numbers of RUNX-2⁺ and osteoprogenitor cells of Osterix⁺ [63]. We also confirmed at the genetic level that the experimental hydrogel could effectively enhance the expression of HIF1A in vitro, demonstrating that our prepared composite hydrogel loaded with USC-EXOs can effectively accelerate formation of H-type vessels and evaluate the quality of the regenerated bone tissue. Nevertheless, our study has yet to reveal the specific mechanism by which the USC-EXOs contribute to osteogenesis and angiogenesis. In future experiments, we will further investigate the signalling pathways and mechanisms of action of experimental hydrogels for bone regeneration.

5. Conclusion

In summary, we propose a strategy to promote bone regeneration with a hydrogel scaffold capable of loading human USC-EXOs. The strategy developed a composite hydrogel composed of two essential components: a GelMA-based photocrosslinkable hydrogel delivery system and exosomes of urine-derived stem cell origin. Due to the presence of USC-EXOs, the hydrogel scaffold evaluated could accelerated bone tissue regeneration by osteogenesis and angiogenesis. The novel bioactive scaffolds we developed appear to have promising clinical applications as a prospering material for bone tissue engineering.

Credit author statement

Wei Lu and Min Zeng: Conceptualization; Methodology; Formal analysis; Investigation; Data Curation; Writing - Original Draft; Visualization, **Wenbin Liu:** Software; Validation; Investigation; Data Curation, **Hui Li, and Yinan Wang** contributed to the data analyses in this experiment, **Xiaolei Fan, Haoyi Wang and Tianliang Ma** contributed to the Investigation in this experiment, **Yihe Hu and Jie Xie:** Writing - Review & Editing; Supervision; Projectadministration; Funding acquisition.

Funding

This study was supported by the National Natural Science Foundation of China (Grant Nos. 81974339), the Key Research and Development program of Hunan Province of China (Grant Nos. 2020GK2008 and 2021GK2012).

Declaration of competing interest

The authors declare that they have no known competing financial interests or personal relationships that could have appeared to influence the work reported in this paper.

Data availability

Data will be made available on request.

Appendix A. Supplementary data

Supplementary data to this article can be found online at <https://doi.org/10.1016/j.mtbio.2023.100569>.

References

- [1] A. Nauth, E. Schemitsch, B. Norris, Z. Nollin, J.T. Watson, Critical-size bone defects: is there a consensus for diagnosis and treatment? *J. Orthop. Trauma* 32 (Suppl 1) (2018).
- [2] F. Simunovic, G. Finkenzeller, Vascularization strategies in bone tissue engineering, *Cells* 10 (7) (2021).
- [3] S. He, J. Fang, C. Zhong, M. Wang, F. Ren, Spatiotemporal delivery of pBMP2 and pVEGF by a core-sheath structured fiber-hydrogel gene-activated matrix loaded with peptide-modified nanoparticles for critical-sized bone defect repair, *Advanced Healthcare Materials* (2022), e2201096.
- [4] C.-Y. Kao, E.T. Papoutsakis, Extracellular vesicles: exosomes, microparticles, their parts, and their targets to enable their biomanufacturing and clinical applications, *Curr. Opin. Biotechnol.* 60 (2019) 89–98.
- [5] H. Rahmoune, P.W. Thompson, J.M. Ward, C.D. Smith, G. Hong, J. Brown, Glucose transporters in human renal proximal tubular cells isolated from the urine of patients with non-insulin-dependent diabetes, *Diabetes* 54 (12) (2005) 3427–3434.
- [6] A. Dörrenhaus, J.I. Müller, K. Golka, P. Jedrusik, H. Schulze, W. Föllmann, Cultures of exfoliated epithelial cells from different locations of the human urinary tract and the renal tubular system, *Arch. Toxicol.* 74 (10) (2000) 618–626.
- [7] J.S. Felix, T.T. Sun, J.W. Littlefield, Human epithelial cells cultured from urine: growth properties and keratin staining, *In Vitro* 16 (10) (1980) 866–874.
- [8] D. Linder, Culture of cells from the urine and bladder washings of adults, *Somat. Cell Genet.* 2 (3) (1976) 281–283.
- [9] Y. Zhang, E. McNeill, H. Tian, S. Soker, K.-E. Andersson, J.J. Yoo, A. Atala, Urine derived cells are a potential source for urological tissue reconstruction, *J. Urol.* 180 (5) (2008) 2226–2233.
- [10] H. Li, X.L. Fan, Y.N. Wang, W. Lu, H. Wang, R. Liao, M. Zeng, J.X. Yang, Y. Hu, J. Xie, Extracellular vesicles from human urine-derived stem cells ameliorate particulate polyethylene-induced osteolysis, *Int. J. Nanomed.* 16 (2021) 7479–7494.
- [11] H. Li, Y. Hu, M. Zeng, J. Yang, X. Fan, Y. Wang, J. Xie, Exosomes from human urine-derived stem cells encapsulated into PLGA nanoparticles for therapy in mice with particulate polyethylene-induced osteolysis, *Front. Med.* 8 (2021), 781449.
- [12] A. Shimoda, K. Ueda, S. Nishiumi, N. Murata-Kamiya, S.-A. Mukai, S.-i. Sawada, T. Azuma, M. Hatakeyama, K. Akiyoshi, Exosomes as nanocarriers for systemic delivery of the *Helicobacter pylori* virulence factor CagA, *Sci. Rep.* 6 (2016), 18346.
- [13] S.-J. Shiue, R.-H. Rau, H.-S. Shiue, Y.-W. Hung, Z.-X. Li, K.D. Yang, J.-K. Cheng, Mesenchymal stem cell exosomes as a cell-free therapy for nerve injury-induced pain in rats, *Pain* 160 (1) (2019) 210–223.
- [14] S.-C. Tao, S.-C. Guo, M. Li, Q.-F. Ke, Y.-P. Guo, C.-Q. Zhang, Chitosan wound dressings incorporating exosomes derived from MicroRNA-126-overexpressing synovium mesenchymal stem cells provide sustained release of exosomes and heal full-thickness skin defects in a diabetic rat model, *Stem Cells Translational Med.* 6 (3) (2017) 736–747.
- [15] C.C. Huang, M. Kang, S. Shirazi, Y. Lu, L.F. Cooper, P. Gajendrareddy, S. Ravindran, 3D Encapsulation and tethering of functionally engineered extracellular vesicles to hydrogels, *Acta Biomater.* 126 (2021) 199–210.
- [16] D. Loessner, C. Meinert, E. Kaemmerer, L.C. Martine, K. Yue, P.A. Levett, T.J. Klein, F.P.W. Melchels, A. Khademhosseini, D.W. Hutmacher, Functionalization, preparation and use of cell-laden gelatin methacryloyl-based hydrogels as modular tissue culture platforms, *Nat. Protoc.* 11 (4) (2016) 727–746.
- [17] K. Yue, G. Trujillo-de Santiago, M.M. Alvarez, A. Tamayol, N. Annabi, A. Khademhosseini, Synthesis, properties, and biomedical applications of gelatin methacryloyl (GelMA) hydrogels, *Biomaterials* 73 (2015) 254–271.
- [18] J.L. Drury, D.J. Mooney, Hydrogels for tissue engineering: scaffold design variables and applications, *Biomaterials* 24 (24) (2003) 4337–4351.
- [19] P.A. Levett, F.P. Melchels, K. Schrobback, D.W. Hutmacher, J. Malda, T.J. Klein, A biomimetic extracellular matrix for cartilage tissue engineering centered on photocurable gelatin, hyaluronic acid and chondroitin sulfate, *Acta Biomater.* 10 (1) (2014) 214–223.
- [20] X.P. Li, L. Zou, O.D. Abodunrin, X.W. Wang, N.P. Huang, Enzyme- and UV-mediated double-network hybrid hydrogels for 3D cell culture application, *Macromol. Biosci.* 21 (11) (2021), e2100189.
- [21] J.-M. Oh, C.C. Venters, C. Di, A.M. Pinto, L. Wan, I. Younis, Z. Cai, C. Arai, B.R. So, J. Duan, G. Dreyfuss, U1 snRNP regulates cancer cell migration and invasion in vitro, *Nat. Commun.* 11 (1) (2020) 1.
- [22] Y. Fan, Z. Yue, E. Lucarelli, G.G. Wallace, Hybrid printing using cellulose nanocrystals reinforced GelMA/HAMA hydrogels for improved structural integration, *Adv Healthc Mater* 9 (24) (2020), e2001410.
- [23] C. Wang, M. Wang, T. Xu, X. Zhang, C. Lin, W. Gao, H. Xu, B. Lei, C. Mao, Engineering bioactive self-healing antibacterial exosomes hydrogel for promoting chronic diabetic wound healing and complete skin regeneration, *Theranostics* 9 (1) (2019) 65–76.
- [24] D. Zhu, Z. Li, K. Huang, T.G. Caranasos, J.S. Rossi, K. Cheng, Minimally invasive delivery of therapeutic agents by hydrogel injection into the pericardial cavity for cardiac repair, *Nat. Commun.* 12 (1) (2021) 1412.

- [25] T. Thakur, J.R. Xavier, L. Cross, M.K. Jaiswal, E. Mondragon, R. Kaunas, A.K. Gaharwar, Photocrosslinkable and elastomeric hydrogels for bone regeneration, *J. Biomed. Mater. Res.* 104 (4) (2016) 879–888.
- [26] Y. Zuo, X. Liu, D. Wei, J. Sun, W. Xiao, H. Zhao, L. Guo, Q. Wei, H. Fan, X. Zhang, Photo-cross-linkable methacrylated gelatin and hydroxyapatite hybrid hydrogel for modularly engineering biomimetic osteon, *ACS Appl. Mater. Interfaces* 7 (19) (2015) 10386–10394.
- [27] J. Gao, X. Ding, X. Yu, X. Chen, X. Zhang, S. Cui, J. Shi, J. Chen, L. Yu, S. Chen, J. Ding, Cell-free bilayered porous scaffolds for osteochondral regeneration fabricated by continuous 3D-printing using nascent physical hydrogel as ink, *Adv Healthc Mater* 10 (3) (2021), e2001404.
- [28] L. Gu, J. Zhang, L. Li, Z. Du, Q. Cai, X. Yang, Hydroxyapatite nanowire composited gelatin cryogel with improved mechanical properties and cell migration for bone regeneration, *Biomed. Mater.* 14 (4) (2019), 045001.
- [29] X. Liu, Y. Chen, A.S. Mao, C. Xuan, Z. Wang, H. Gao, G. An, Y. Zhu, X. Shi, C. Mao, Molecular recognition-directed site-specific release of stem cell differentiation inducers for enhanced joint repair, *Biomaterials* 232 (2020), 119644.
- [30] H. Hu, L. Dong, Z. Bu, Y. Shen, J. Luo, H. Zhang, S. Zhao, F. Lv, Z. Liu, miR-23a-3p-abundant small extracellular vesicles released from Gelma/nanoclay hydrogel for cartilage regeneration, *J. Extracell. Vesicles* 9 (1) (2020), 1778883.
- [31] M. Diba, G.L. Koons, M.L. Bedell, A.G. Mikos, 3D printed colloidal biomaterials based on photo-reactive gelatin nanoparticles, *Biomaterials* 274 (2021), 120871.
- [32] B. Velasco-Rodriguez, T. Diaz-Vidal, L.C. Rosales-Rivera, C.A. Garcia-Gonzalez, C. Alvarez-Lorenzo, A. Al-Modlej, V. Dominguez-Arca, G. Prieto, S. Barbosa, J.F.A. Soltero Martinez, P. Taboada, Hybrid methacrylated gelatin and hyaluronic acid hydrogel scaffolds. Preparation and systematic characterization for prospective tissue engineering applications, *Int. J. Mol. Sci.* 22 (13) (2021).
- [33] A.R. Osi, H. Zhang, J. Chen, Y. Zhou, R. Wang, J. Fu, P. Muller-Buschbaum, Q. Zhong, Three-dimensional-printable thermo/photo-cross-linked methacrylated chitosan-gelatin hydrogel composites for tissue engineering, *ACS Appl. Mater. Interfaces* 13 (19) (2021) 22902–22913.
- [34] W. Wei, Y. Ma, X. Zhang, W. Zhou, H. Wu, J. Zhang, J. Lin, C. Tang, Y. Liao, C. Li, X. Wang, X. Yao, Y.W. Koh, W. Huang, H. Ouyang, Biomimetic joint paint for efficient cartilage repair by simultaneously regulating cartilage degeneration and regeneration in pigs, *ACS Appl. Mater. Interfaces* 13 (46) (2021) 54801–54816.
- [35] Y. Cao, Y. Xu, C. Chen, H. Xie, H. Lu, J. Hu, Local delivery of USC-derived exosomes harboring ANGPTL3 enhances spinal cord functional recovery after injury by promoting angiogenesis, *Stem Cell Res. Ther.* 12 (1) (2021) 20.
- [36] C. Cai, X. Zhang, Y. Li, X. Liu, S. Wang, M. Lu, X. Yan, L. Deng, S. Liu, F. Wang, C. Fan, Self-healing hydrogel embodied with macrophage-regulation and responsive-gene-silencing properties for synergistic prevention of peritendinous adhesion, *Adv. Mater.* 34 (5) (2022), e2106564.
- [37] X. He, W. Liu, Y. Liu, K. Zhang, Y. Sun, P. Lei, Y. Hu, Nano artificial periosteum PLGA/MgO/Quercetin accelerates repair of bone defects through promoting osteogenic - angiogenic coupling effect via Wnt/ β -catenin pathway, *Materials Today. Bio.* 16 (2022), 100348.
- [38] A.G. Kurian, R.K. Singh, K.D. Patel, J.-H. Lee, H.-W. Kim, Multifunctional GelMA platforms with nanomaterials for advanced tissue therapeutics, *Bioact. Mater.* 8 (2022) 267–295.
- [39] Y. Liu, T. Li, M. Sun, Z. Cheng, W. Jia, K. Jiao, S. Wang, K. Jiang, Y. Yang, Z. Dai, L. Liu, G. Liu, Y. Luo, ZIF-8 modified multifunctional injectable photopolymerizable GelMA hydrogel for the treatment of periodontitis, *Acta Biomater.* 146 (2022) 37–48.
- [40] Y. Sun, T. Liu, H. Hu, Z. Xiong, K. Zhang, X. He, W. Liu, P. Lei, Y. Hu, Differential effect of tantalum nanoparticles versus tantalum micron particles on immune regulation, *Materials Today. Bio.* 16 (2022), 100340.
- [41] M. Yuan, K. Liu, T. Jiang, S. Li, J. Chen, Z. Wu, W. Li, R. Tan, W. Wei, X. Yang, H. Dai, Z. Chen, GelMA/PEGDA microneedles patch loaded with HUVECs-derived exosomes and Tazarotene promote diabetic wound healing, *J. Nanobiotechnol.* 20 (1) (2022) 147.
- [42] H. Wu, Y. Shang, W. Sun, X. Ouyang, W. Zhou, J. Lu, S. Yang, W. Wei, X. Yao, X. Wang, X. Zhang, Y. Chen, Q. He, Z. Yang, H. Ouyang, Seamless and early gap healing of osteochondral defects by autologous mosaicplasty combined with bioactive supramolecular nanofiber-enabled gelatin methacryloyl (BSN-GelMA) hydrogel, *Bioact. Mater.* 19 (2023).
- [43] N. Enomoto, S. Homma, N. Inase, Y. Kondoh, T. Saraya, H. Takizawa, Y. Inoue, H. Ishii, Y. Taguchi, S. Izumi, Y. Yamano, Y. Tanino, Y. Nishioka, M. Toyoshima, K. Yokomura, S. Imokawa, N. Koshimizu, T. Sano, T. Akamatsu, H. Mukae, M. Kato, N. Hamada, H. Chiba, S. Akagawa, S. Muro, H. Uruga, H. Matsuda, Y. Kaida, M. Kanai, K. Mori, M. Masuda, H. Hozumi, T. Fujisawa, Y. Nakamura, N. Ogawa, T. Suda, Prospective nationwide multicentre cohort study of the clinical significance of autoimmune features in idiopathic interstitial pneumonias, *Thorax* 77 (2) (2022) 143–153.
- [44] W. Ma, X. Zhang, Y. Liu, L. Fan, J. Gan, W. Liu, Y. Zhao, L. Sun, Polydopamine decorated microneedles with Fe-MS-C-Derived nanovesicles encapsulation for wound healing, *Adv. Sci.* 9 (13) (2022), e2103317.
- [45] J. Shen, A. Chen, Z. Cai, Z. Chen, R. Cao, Z. Liu, Y. Li, J. Hao, Exhausted local lactate accumulation via injectable nanozyme-functionalized hydrogel microsphere for inflammation relief and tissue regeneration, *Bioact. Mater.* 12 (2022) 153–168.
- [46] L. Cai, S. Liu, J. Guo, Y.G. Jia, Polypeptide-based self-healing hydrogels: design and biomedical applications, *Acta Biomater.* 113 (2020) 84–100.
- [47] X. Shen, S. Li, X. Zhao, J. Han, J. Chen, Z. Rao, K. Zhang, D. Quan, J. Yuan, Y. Bai, Dual-crosslinked regenerative hydrogel for sutureless long-term repair of corneal defect, *Bioact. Mater.* 20 (2023) 434–448.
- [48] Y. Yang, Y. Zhang, Y. Min, J. Chen, Preparation of methacrylated hyaluronate/methacrylated collagen sponges with rapid shape recovery and orderly channel for fast blood absorption as hemostatic dressing, *Int. J. Biol. Macromol.* 222 (Pt A) (2022) 30–40.
- [49] Y. Yang, M. Wang, S. Yang, Y. Lin, Q. Zhou, H. Li, T. Tang, Bioprinting of an osteocyte network for biomimetic mineralization, *Biofabrication* 12 (4) (2020), 045013.
- [50] Z. Ni, S. Zhou, S. Li, L. Kuang, H. Chen, X. Luo, J. Ouyang, M. He, X. Du, L. Chen, Exosomes: roles and therapeutic potential in osteoarthritis, *Bone Res* 8 (2020) 25.
- [51] Q. Zhou, Y. Cai, Y. Jiang, X. Lin, Exosomes in osteoarthritis and cartilage injury: advanced development and potential therapeutic strategies, *Int. J. Biol. Sci.* 16 (11) (2020) 1811–1820.
- [52] G.R. Sutherland, A.D. Bain, Culture of cells from the urine of newborn children, *Nature* 239 (5369) (1972) 231.
- [53] C.Y. Chen, W. Du, S.S. Rao, Y.J. Tan, X.K. Hu, M.J. Luo, Q.F. Ou, P.F. Wu, L.M. Qing, Z.M. Cao, H. Yin, T. Yue, C.H. Zhan, J. Huang, Y. Zhang, Y.W. Liu, Z.X. Wang, Z.Z. Liu, J. Cao, J.H. Liu, C.G. Hong, Z.H. He, J.X. Yang, S.Y. Tang, J.Y. Tang, H. Xie, Extracellular vesicles from human urine-derived stem cells inhibit glucocorticoid-induced osteonecrosis of the femoral head by transporting and releasing pro-angiogenic DMBT1 and anti-apoptotic TIMP1, *Acta Biomater.* 111 (2020) 208–220.
- [54] N. Di Maggio, A. Banfi, The osteo-angiogenic signaling crosstalk for bone regeneration: harmony out of complexity, *Curr. Opin. Biotechnol.* 76 (2022), 102750.
- [55] M. Dzamukova, T.M. Brunner, J. Miotla-Zarebska, F. Heinrich, L. Brylka, M.-F. Mashreghi, A. Kusumbe, R. Kühn, T. Schinke, T.L. Vincent, M. Löhning, Mechanical forces couple bone matrix mineralization with inhibition of angiogenesis to limit adolescent bone growth, *Nat. Commun.* 13 (1) (2022) 3059.
- [56] Y. He, W. Wang, S. Lin, Y. Yang, L. Song, Y. Jing, L. Chen, Z. He, W. Li, A. Xiong, K.W.K. Yeung, Q. Zhao, Y. Jiang, Z. Li, G. Pei, Z.-Y. Zhang, Corrigendum to 'Fabrication of a bio-instructive scaffold conferred with a favorable microenvironment allowing for superior implant osseointegration and accelerated in situ vascularized bone regeneration via type H vessel formation' [Bioactive Materials, Volume 9 (March 2022) Page 491-507], *Bioact. Mater.* 20 (2023) 164.
- [57] Y. Zeng, C. Huang, D. Duan, A. Lou, Y. Guo, T. Xiao, J. Wei, S. Liu, Z. Wang, Q. Yang, L. Zhou, Z. Wu, L. Wang, Injectable temperature-sensitive hydrogel system incorporating deferoxamine-loaded microspheres promotes H-type blood vessel-related bone repair of a critical size femoral defect, *Acta Biomater.* 153 (2022) 108–123.
- [58] A.N. Rindone, X. Liu, S. Farhat, A. Perdomo-Pantoja, T.F. Witham, D.L. Coutu, M. Wan, W.L. Grayson, Quantitative 3D imaging of the cranial microvascular environment at single-cell resolution, *Nat. Commun.* 12 (1) (2021) 6219.
- [59] Y. Zhai, K. Schilling, T. Wang, M. El Khatib, S. Vinogradov, E.B. Brown, X. Zhang, Spatiotemporal blood vessel specification at the osteogenesis and angiogenesis interface of biomimetic nanofiber-enabled bone tissue engineering, *Biomaterials* 276 (2021), 121041.
- [60] A.P. Kusumbe, S.K. Ramasamy, R.H. Adams, Coupling of angiogenesis and osteogenesis by a specific vessel subtype in bone, *Nature* 507 (7492) (2014) 323–328.
- [61] Z. Cui, H. Wu, Y. Xiao, T. Xu, J. Jia, H. Lin, R. Lin, K. Chen, Y. Lin, K. Li, X. Wu, C. Li, B. Yu, Endothelial PDGF-BB/PDGFR- β signaling promotes osteoarthritis by enhancing angiogenesis-dependent abnormal subchondral bone formation, *Bone Research* 10 (1) (2022) 58.
- [62] J. Mi, J.-K. Xu, Z. Yao, H. Yao, Y. Li, X. He, B.-Y. Dai, L. Zou, W.-X. Tong, X.-T. Zhang, P.-J. Hu, Y.C. Ruan, N. Tang, X. Guo, J. Zhao, J.-F. He, L. Qin, Implantable electrical stimulation at dorsal root ganglions accelerates osteoporotic fracture healing via calcitonin gene-related peptide, *Adv. Sci.* 9 (1) (2022), e2103005.
- [63] N. Tang, L. Wang, J. Esko, F.J. Giordano, Y. Huang, H.-P. Gerber, N. Ferrara, R.S. Johnson, Loss of HIF-1alpha in endothelial cells disrupts a hypoxia-driven VEGF autocrine loop necessary for tumorigenesis, *Cancer Cell* 6 (5) (2004) 485–495.